



LAWRENCE
LIVERMORE
NATIONAL
LABORATORY

Plasma Flow Reactor Chemical Kinetics: A Method Toward Optimizing Nano-Manufacturing and Laser Inertial Fusion Energy Strategies

B. Koroglu, M. Mehl, J. Crowhurst, J. M. Zaug, T.
Rose, H. Radousky, M. Armstrong

May 17, 2018

Plasma Physics and Controlled Fusion

Disclaimer

This document was prepared as an account of work sponsored by an agency of the United States government. Neither the United States government nor Lawrence Livermore National Security, LLC, nor any of their employees makes any warranty, expressed or implied, or assumes any legal liability or responsibility for the accuracy, completeness, or usefulness of any information, apparatus, product, or process disclosed, or represents that its use would not infringe privately owned rights. Reference herein to any specific commercial product, process, or service by trade name, trademark, manufacturer, or otherwise does not necessarily constitute or imply its endorsement, recommendation, or favoring by the United States government or Lawrence Livermore National Security, LLC. The views and opinions of authors expressed herein do not necessarily state or reflect those of the United States government or Lawrence Livermore National Security, LLC, and shall not be used for advertising or product endorsement purposes.

Experimental and Modeling Study of Chemical-Based Strategies for Mitigating Dust Formation in Fusion Reactors

Journal of Plasma Physics and Controlled Fusion

LLNL-JRNL-751484

This work was performed under the auspices of the U.S. Department of Energy by Lawrence Livermore National Laboratory under Contract DE-AC52-07NA27344.

Batikan Koroglu*, Marco Mehl[§], Jonathan C. Crowhurst, Joseph M. Zaug,
Timothy P. Rose, Harry B. Radousky, and Michael R. Armstrong
Lawrence Livermore National Laboratory, Livermore CA, 94550, USA

[§] Present address: Department of Chemistry, Materials, and Chemical Engineering,
Politecnico di Milano

**Corresponding Author: koroglu1@llnl.gov*

Abstract:

We studied carbon/hydrogen/oxygen chemical kinetics at time scales and thermal conditions relevant to fusion energy applications using a custom-built plasma flow reactor to investigate chemical-based strategies for eliminating carbon dust formation in fusion reactors. Acetylene and oxygen gases under varying conditions of initial concentrations are injected into an inductively coupled argon plasma where complete molecular dissociation occurs. The evolution of chemical species is investigated along the plasma flow reactor as a function of temperature and residence time. Atomized species of C, H, and O cool from 5000 K to 1000 K within 30 ms at atmospheric pressures. We employed optical emission and infrared absorption spectroscopy to measure the reaction intermediates (e.g. C₂) and products (e.g. C₂H₂). Chemical equilibrium models are inadequate to describe the evolution of carbon molecular products, and thus a chemical kinetics model is developed. In both experiments and kinetic modelling, we find that the addition of oxygen in 1:1 proportion to carbon strongly favors the formation of CO, preventing the formation of acetylene (an important soot precursor) in less than 10 milliseconds. The kinetics model is also used to perform a reaction sensitivity and a rate of production analyses to identify the rate determining steps and the major chemical pathways that control the acetylene production/consumption. The results demonstrate the feasibility of chemical-based strategies for eliminating the formation of carbonaceous particles in fusion energy reactors.

1. INTRODUCTION

Hydrogen isotope retention to carbonaceous or metallic components of fusion devices results in the formation of radioactive dust due to plasma-surface interactions, which poses operational and safety concerns in the development of fusion energy reactors¹⁻⁴. The dust affects plasma operation, deteriorating its stability and overall performance. Therefore, understanding the dust formation mechanism in fusion environments is crucial to prevent the associated contamination issues. Prior studies of dust formation mechanisms included *post mortem* analysis of particles (e.g. carbon, tungsten, beryllium) collected from tokamaks^{1,5,6} and small-scale experimental setups (e.g. argon-acetylene plasma torches)^{5,7} designed to simulate the fusion reactor environment. Electron microscope images of dust from both types of tests revealed substantial similarities. Spherical particles with fractal columnar growth were attributed to particle growth from hydrocarbon precursors in the gas phase^{8,9}. Additional laboratory-scale experiments at conditions relevant to plasma-wall interactions in fusion reactors are necessary to better understand the mechanisms of dust formation and to accurately predict the rate and amount of dust formation.

In the field of inertial confinement fusion (ICF), a technical approach where carbon dust could be detrimental involves the injection of a continuous input stream of fusion target materials (including tritium and carbon) into a large chamber analogous to the National Ignition Facility target chamber at LLNL^{10,11}. Radioactive hydrocarbons would condense as solids on the inner wall of the chamber, leading to costly contamination issues. Although different methods have been investigated to remove carbon deposits from plasma-facing components of fusion reactors (e.g. chemical oxidation, laser ablation¹²⁻¹⁶), simultaneous operation and cleaning by means of chemical oxidation was not tested before. A proposed method to prevent hydrocarbon accumulation during reactor operation is to add oxygen to the input stream of gasses to generate carbon monoxide/dioxide instead of carbon dust. We examine the proposed mitigation strategy using a custom-built atmospheric pressure plasma flow reactor¹⁷ and investigate the mechanisms of carbon dust formation at temperatures relevant to plasma-wall interactions in fusion reactors.

The mechanism of sub-micron carbonaceous particle formation (i.e. soot) from gaseous hydrocarbon precursors (e.g. acetylene) was studied before during combustion/pyrolysis processes¹⁸⁻²³. It was shown that polycyclic aromatic hydrocarbons (PAHs) grow towards the soot particles via the H-Abstraction-C₂H₂ (acetylene)-Addition mechanism (HACA). The process starts with the creation of the first aromatic ring (i.e. benzene) via combination of C₄H₅ with C₂H₂ (or via

combination of two C_3H_3 radicals) and a production of a hydrogen radical. After that, the benzene forms a naphthalene molecule (i.e. two fused benzene rings) through two successive HACA reactions. The same repetitive cyclisation continues and produces a pyrene molecule that includes four fused benzene rings. The genesis of soot is assumed to result from the condensation of two pyrene molecules²⁴. Previous research showed that soot formation in laboratory plasmas occurs by the same HACA mechanism at moderate pressures (e.g. $P > 200$ mbar)^{24,25} due to rapid thermalization of species as a result of increased number of collisions. It was also shown that acetylene plays an equally important role as a soot precursor in low pressure plasmas ($P = 0.27$ mbar) where the reactions between acetylene and ionic species contribute to the growth of carbonaceous clusters^{25,26}. Since acetylene is the key molecule in carbon dust formation, we monitor acetylene formation in our plasma flow reactor as a function of input carbon/oxygen concentration to investigate the proposed method of preventing carbon dust formation in ICF environments¹⁰ via oxygen addition to the input stream of gasses.

Acetylene is also well-suited as a starting material for studying carbonaceous particle formation in laboratory plasmas due to its high carbon/hydrogen content^{27,28}. Therefore, in this study we inject acetylene gas into our inductively coupled argon plasma torch and investigate the evolution of chemical species along the flow reactor as a function of temperature and residence time. Low concentrations of acetylene and oxygen gasses (e.g. 54 ppm to 540 ppm) are used to ensure the molecules are fully dissociated into their constituent elements as they pass through the argon plasma. UV/VIS emission spectroscopy is used to monitor the high-temperature formation of diatomic carbon molecules from carbon atoms resulting from acetylene decomposition. Infrared absorption spectroscopy is used to measure the formation of new C_2H_2 molecules downstream of the plasma, and to monitor how C_2H_2 formation varies with input oxygen concentration. We also assembled a chemical kinetics model for the C/H/O system, performed a reaction sensitivity and a rate of production analyses to determine the important reactions controlling the output acetylene yield, and validated the model predictions using our experimental results. The model provides a predictive capability that can be used to begin optimizing extreme condition performance within a fusion reactor environment.

2. EXPERIMENTAL MEASUREMENTS

A plasma flow reactor¹⁷ is used as a proxy to generate thermodynamic conditions similar to the outer and thermally cooler regions of proposed fusion energy ignition chambers^{10,11}. In terms

of mass-flow time-scale (tens of milliseconds), temperature range ($6000\text{ K} < T < 300\text{ K}$), and experimental convenience, the combination of an inductively coupled plasma and a laminar flow reactor is well-suited to investigate the chemical kinetic pathways leading to dust formation in fusion reactors. Experimental details are illustrated in Figure 1. The reactor consists of a 20 mm OD inductively coupled plasma (ICP) torch attached to a 40 mm OD quartz tube by means of an adapter. The outermost, central, and innermost argon flow rates through the ICP torch were set to 18, 0, and 0.3 l/min, respectively. Two additional flow controllers (Omega, FMA 2616A and FMA-2604A) were used in this study to introduce small amounts of acetylene and oxygen gasses into the argon plasma. Acetylene amount was varied between 1 and 10 ml/min, whereas the oxygen amount ranged from 0 to 15 ml/min. These settings yielded acetylene input concentrations between 54 and 540 ppm. Our flow controllers were also equipped with absolute pressure sensors to monitor the atmospheric pressure during the course of our experiments.

A moving stage is vertically positioned next to the plasma flow reactor to accommodate optical components. Labview-code was written to control a stepper-motor to adjust stage position with high precision ($\pm 0.01\text{ cm}$). The UV/VIS emission spectra of hot gases ($T \sim 3500\text{ K}$) were measured at 4 cm distance from the end of the RF coil to detect diatomic carbon and to determine temperature. In addition, infrared spectra near 3000 nm (3333 cm^{-1}) were recorded to detect recombined C_2H_2 molecules at 16 and 116 cm positions along the flow reactor where measured temperatures were 950 K and 320 K respectively. Additional experimental details are discussed in the next section.

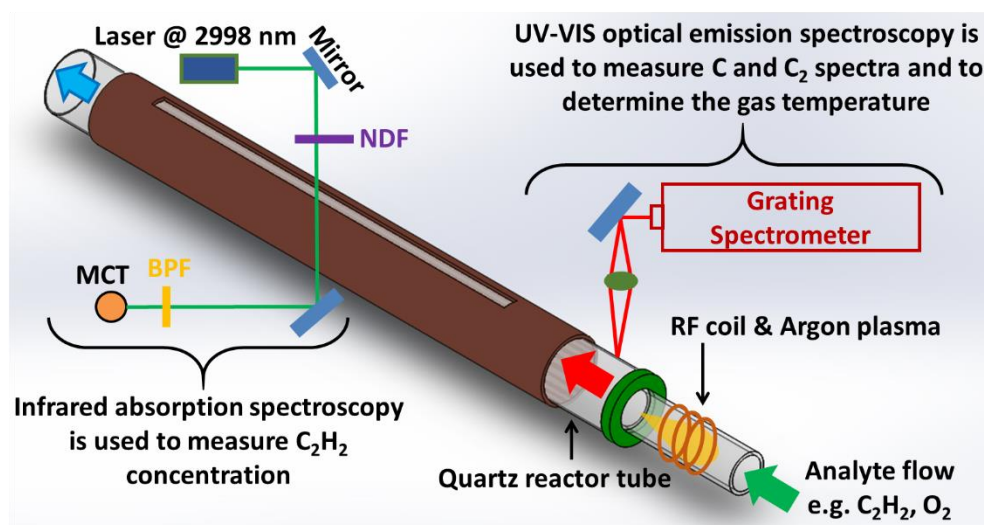


Figure 1. The schematic of the plasma flow reactor experimental setup.
(NDF: Neutral density filter, MCT: Mercury Cadmium Telluride Detector, BPF: Band pass filter)

2.1 C₂H₂ Concentration Measurement

The detection of stable acetylene downstream of the plasma flow reactor was performed using laser absorption spectroscopy. C₂H₂ has a structurally resolved strong absorption near 2998 nm. A fixed wavelength laser absorption diagnostic scheme was developed by Stranic and Hanson²⁹ in this region to measure C₂H₂ concentration at high temperatures ($T > 1000$ K) during the pyrolysis of higher order hydrocarbons. Other species such as CO, CO₂, CH₄, and H₂O can produce interference absorption and hence lead to uncertainties in C₂H₂ concentration measurements. Therefore, the measurements were performed at two wavelengths with a very narrow line spacing ($\lambda_{\text{valley}} = 2997.8$ nm and $\lambda_{\text{peak}} = 2998.0$ nm). Optical absorption measured at the valley wavelength was subtracted from absorption at the peak wavelength. In this way, interferences were eliminated because other species had broad and unstructured absorption spectra at the chosen wavelength pair. The resulting differential absorption was used to determine the C₂H₂ concentration. Empirical formulations giving the dependence of absorption cross sections of acetylene for the chosen wavelength pair were reported as a function of temperature and pressure ($1070 < T < 1720$ K and $0.8 < P < 4.0$ atm)²⁹. These reported cross sections were used here to obtain absolute C₂H₂ concentrations from measured infrared absorption at λ_{peak} and λ_{valley} .

An example acetylene concentration measurement was reported in our recent publication¹⁷. We used the same laser and detector configuration in the present study. Infrared light from a continuous-wave distributed feedback inter-band cascade laser (Nanoplus DFB ICL) was modulated near 2998 nm to measure acetylene (C₂H₂) absorption. The position-controlled laser beam passes through the flow reactor and is incident on a thermoelectrically cooled HgCdTe (MCT) detector (Vigo Systems PVI-3TE-4). The ratio of sample and reference signal intensity ($I_{\text{sample}}/I_{\text{ref}}$) was measured to obtain the C₂H₂ mole fraction from the Beer-Lambert law:

$$\alpha_{\lambda} = -\ln\left(\frac{I_{\text{Sample}}}{I_{\text{ref}}}\right)_{\lambda} = \sigma(\lambda, T, P) \frac{P_{\text{tot}}}{RT} \chi L \quad (1)$$

where α_{λ} is the absorbance at wavelength λ , σ [cm²/mol] is the absorption cross section, P_{tot} [atm] is the total pressure within the system, and T [K] is the temperature of the gas. L [cm] is the optical path length (flow reactor inner diameter is 3.7 cm), R is the universal gas constant, and χ is the mole fraction of the absorbing species. Reference intensity, $[I_{\text{ref}}]$, was measured when only argon was flowing through the reactor. Research grade argon (99.999%) was used during the tests.

The room temperature absorption coefficient of acetylene measured using the plasma flow reactor (when the RF generator was not in operation) is shown in Figure 2. The results are compared to selected measurements of Stranic and Hanson²⁹. Very good agreement was observed. Our measurements were taken using 536 ppm of acetylene in argon buffer gas at 296 K. Similar spectral measurements were performed for a range of C₂H₂ concentrations (54 ppm < X_{C₂H₂} < 540 ppm) to compare the measured concentrations with those determined from the flow rate settings on the digital flow controllers. The two measurements agreed to within ±2%.

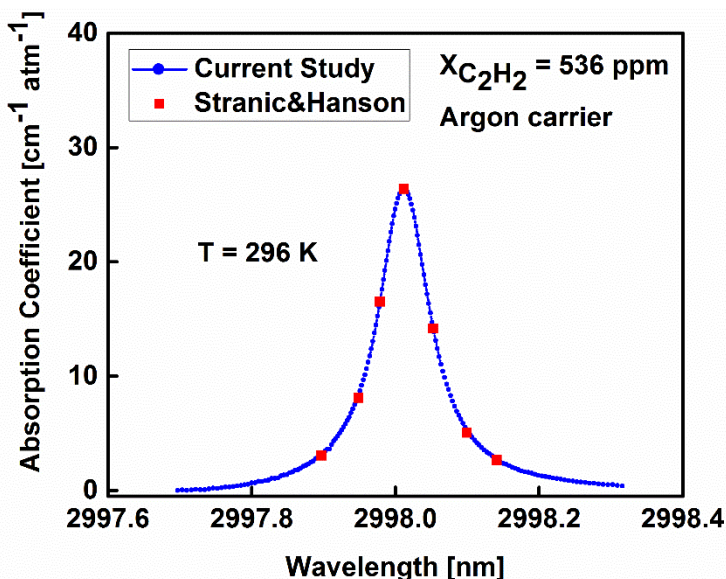


Figure 2. Comparison of absorption coefficients of acetylene with literature data at 296 K²⁹.

2.2 Emission Measurements of Diatomic Carbon

A low resolution (FWHM=0.5 nm) spectrometer (Ocean optics, USB 2000+XR1-ES) recorded vibrational sequences ($\Delta v = 0, \pm 1$) of diatomic carbon ($d^3\Pi_g \rightarrow a^3\Pi_u$) between 440 and 580 nm. Oxygen concentration was adjusted during these measurements to determine corresponding variations in relative C₂ concentrations. Three sample spectra that are recorded 4 cm downstream of the RF coil are shown in Figure 3. Diatomic carbon emission intensity decreased with increasing oxygen concentration. Correlations to oxygen concentration are discussed below in Section 4.2. We also recorded the emission spectra of carbon atoms centered at 247.8 nm as well as the emission of the diatomic carbon as a function of distance along the flow reactor. We observed that the diatomic carbon molecules were fully dissociated into carbon atoms at 1.7 cm downstream of the RF coil. The absence of diatomic carbon at 1.7 cm indicates complete dissociation of acetylene

as it passes through the argon plasma. Molecular emission of C_2 was observed once again 4 cm downstream of the plasma torch due to the recombination of carbon atoms at cooler temperatures.

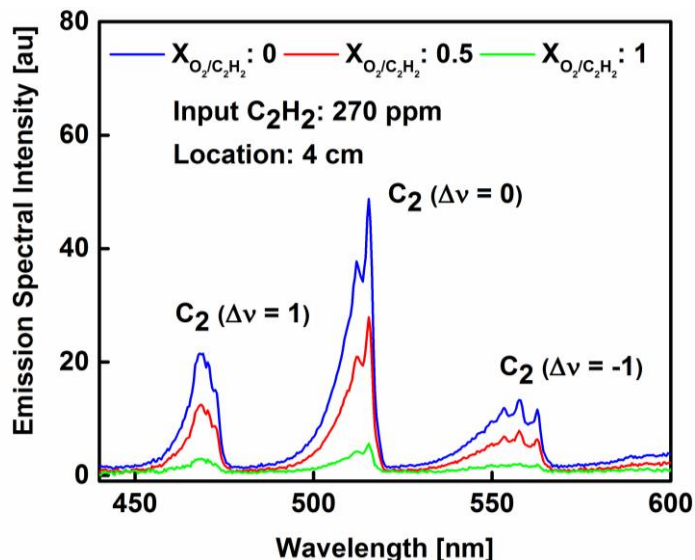


Figure 3 Molecular emission intensities of C_2 for various concentrations of oxygen. Input concentration of C_2H_2 was fixed at 270 ppm, whereas oxygen amount was varied.

2.3 Temperature Measurements

The closely spaced rotational transitions of diatomic molecules (e.g. C_2 and AlO) enable the determination of the gas kinetic temperature^{30–32}. In our previous works^{17,33}, we measured the rotational spectra of the AlO molecules in addition to the purely electronic transitions of Fe atoms and determined the rotational and electron temperatures, respectively. The measurements were taken at multiple locations 2 cm after the end of the RF coil. The two temperatures were consistent within the measurement uncertainties, +/- 10%. Therefore, local thermodynamic equilibrium was established between different degrees of freedom for different species. In this study, we measure the rotational temperature using the rotational transitions of diatomic carbon molecules and report that as the gas kinetic temperature within our plasma-flow reactor.

A high-resolution grating spectrometer (JY Horiba, HR 460; FWHM spectral resolution = 0.05 nm) recorded emission spectra from C_2 molecules. Molecular emission measurements enabled temperature determinations to be made relatively near (4 cm) to the RF coil. The measured spectral intensities and line positions were calibrated using a halogen lamp (Ocean optics, HL-3 plus-CAL-EXT) and a neon lamp, respectively. Parigger et al.³⁴ published line strength tables for various molecules (e.g. C_2 , CN, AlO) and a Nelder Mead Temperature (NMT) least squares fitting program for plasma applications. We used this tool to determine temperatures from the measured spectra. The modeled fit to the measured C_2 emission spectra is shown in Figure 4. Temperature was

determined to be 3534 K \pm 353 K. (Temperatures determined using this method have a reported uncertainty of \pm 10% ³⁴.) We performed similar data fittings across different C₂ emission spectral regions; variations in calculated temperatures were well within expected uncertainties. The C₂ emission spectra were also recorded at the same location along the reactor when oxygen and acetylene gases were input together to the argon plasma. The variation in calculated temperatures as a function of analyte concentration ranged from 3500 K to 3700 K and is, again, within the uncertainty of the measurements (\pm 10%).

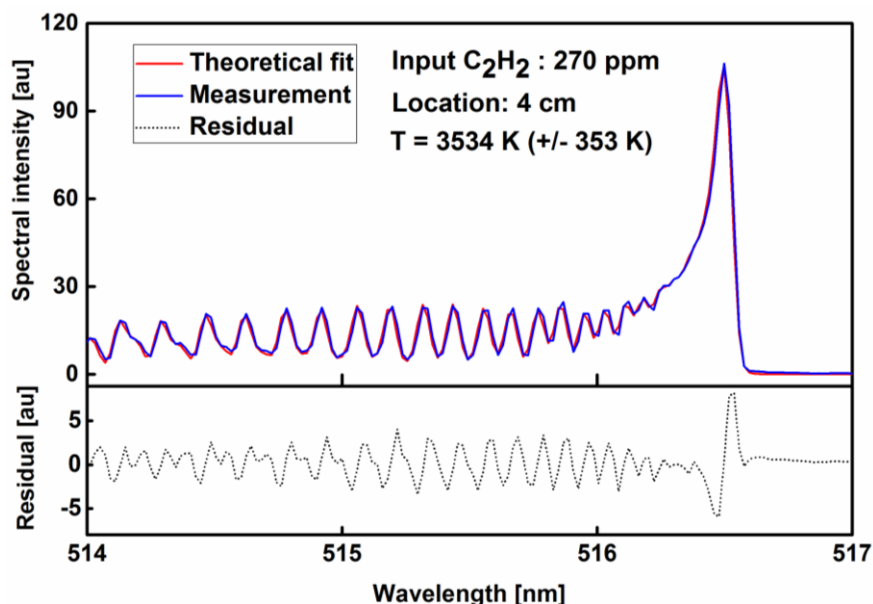


Figure 4. Example emission spectra of diatomic carbon. The determined temperature (by comparison to a theoretical calculation) is 3534 \pm 353 K ³⁴. The residual curve (i.e. measurement minus fit) is plotted at the bottom of the Figure.

3. KINETIC AND EQUILIBRIUM MODELS

A detailed reaction mechanism was assembled to describe the high temperature decomposition and recombination kinetics of acetylene (C₂H₂) in argon buffer gas in high/low oxygen environments. Acetylene is completely dissociated into its atomic species after passing through the inductively coupled argon plasma. Reaction rates describing the dissociation of species such as C₂H₂, C₂, CH, and CO are taken from the literature ³⁵⁻⁴³. Those reaction pathways are summarized in Table 1 together with their associated rate constants, *k*, from the modified Arrhenius form,

$$k = AT^n \exp\left(\frac{E_{act}}{RT}\right), \quad (2)$$

where A is the pre-exponential factor [$\text{cm}^3/\text{mol s}$], T is the temperature [K], E_{act} is the activation energy [cal/mol], n is the temperature power constant, and R is the universal gas constant (1.987 cal/mol K). The chemistry at lower temperatures ($T < 3500$ K) is expected to follow reactions similar to a combustion system involving radicals (e.g. CH) and formation of stable molecules (e.g. CH_4 , C_2H_2 , etc.). As a result, we combined the reactions and species listed in Table 1 with the detailed kinetic mechanism of Miller and Klippenstein⁴⁴. In addition, we included other reactions to describe the formation of aromatic species with one (e.g. C_6H_6)^{45,46} and two rings (C_{10}H_8)⁴⁷. Our assembled reaction mechanism includes 756 reactions and 128 chemical species.

Table 1. Reactions and kinetic parameters adopted in the kinetic mechanism to describe the high temperature decomposition/recombination of C/H/O atoms.

Reaction	A [$\text{cm}^3/\text{mol s}$]	n	E_a [cal/mol]	Reference
$\text{CO} \rightleftharpoons \text{C} + \text{O}$	1.7E+21	-1.5	113592	Hanson ³⁵
$\text{CH} + \text{CH} \rightleftharpoons \text{C}_2\text{H}_2$	1.20E+14	0	0	Braun et al. ³⁶
$\text{CH} + \text{M} \rightleftharpoons \text{C} + \text{H} + \text{M}$	1.90E+14	0	66969	Dean and Hanson ³⁷
$\text{C} + \text{H}_2 \rightleftharpoons \text{CH}_2$	1.24E+13	0	113	Harding et al. ³⁸
$\text{C}_2 + \text{M} \rightleftharpoons \text{C} + \text{C} + \text{M}$	1.50E+16	0	142284	
$\text{C}_2 + \text{C}_2 \rightleftharpoons \text{C} + \text{C}_3$	3.20E+14	0	0	Kruse and Roth ³⁹
$\text{C}_2 + \text{C}_3 \rightleftharpoons \text{C} + \text{C}_4$	3.20E+14	0	0	
$\text{C}_2 + \text{C}_4 \rightleftharpoons \text{C} + \text{C}_5$	3.20E+14	0	0	
$\text{C} + \text{CH}_2 \rightleftharpoons \text{CH} + \text{CH}$	1.62E+12	0	46898	Mayer et al. ⁴⁰
$\text{CO} + \text{M} \rightleftharpoons \text{C} + \text{O} + \text{M}$	4.29E+27	-3.10	256350	Mick et al. ⁴¹
$\text{CO} + \text{C} + \text{M} \rightleftharpoons \text{C}_2\text{O} + \text{M}$	2.29E+16	0	0	Husain and Kirsch ⁴²
$\text{CO}_2 + \text{C} \rightleftharpoons \text{CO} + \text{CO}$	6.02E+09	0	0	Husain and Young ⁴³

In order to calculate chemical evolution along the length and central axial regions of the plasma flow reactor, three dimensional computational fluid dynamics (CFD) simulations of the flow-field and temperature were performed using Starccm⁴⁸ as described in our recent studies^{17,33}. Temperature as a function of residence time was obtained from the CFD simulations using the temperature history of a parcel of gas injected into the plasma torch. The extracted information (temperature vs residence time at atmospheric pressure) was imposed as a boundary condition for chemical kinetics calculations performed using Chemkin-Pro⁴⁹.

In this study, we also show equilibrium model predictions, because the residence time of the gas through our flow reactor is very long ($\Delta t > 10$ ms) at very high temperatures ($T > 2250$ K). Other experimental setups used to study kinetics of chemical reactions at high temperatures (e.g. shock tubes) have only a few milliseconds of test times⁵⁰. In addition, our experiments are

performed at atmospheric pressures. The high collision rate between various species (neutrals, ionized, electrons) at atmospheric pressures enables rapid thermalization of the system. Therefore, the long residence time at elevated temperatures and atmospheric pressures might be adequate to achieve chemical equilibrium products, since the kinetics of reactions non-linearly increase with temperature. As a result, equilibrium model calculations were also performed in the current study based on the minimization of the Gibbs free energy approach.

Thermodynamic properties (e.g. enthalpy, entropy) were taken from the Burcat thermochemistry database⁵¹ and used in chemical equilibrium and kinetic simulations. The chemical equilibrium and kinetic model predictions are compared to the experimental measurements in the results and discussion section.

4. RESULTS AND DISCUSSION

Measured temperatures and CFD model predictions are plotted in Figure 5. Temperature at the 16 cm location was measured using a Type-K thermocouple (Omega Industries) in the center of the flow field. At high temperatures (e.g. $T > 1000$ K), radiation heat loss from the thermocouple bead becomes significant, resulting in a substantial difference between the thermocouple recording and actual gas temperature. Therefore, these heat losses were accounted for using the Stefan-Boltzmann law to determine gas temperatures based on the thermocouple readings. For the highest thermocouple reading reported, the calculated gas temperature (e.g. $T_{\text{gas}} \sim 1000$ K) was, at most, 12.5% above the measured value (e.g. $T_{\text{thermocouple}} \sim 875$ K).

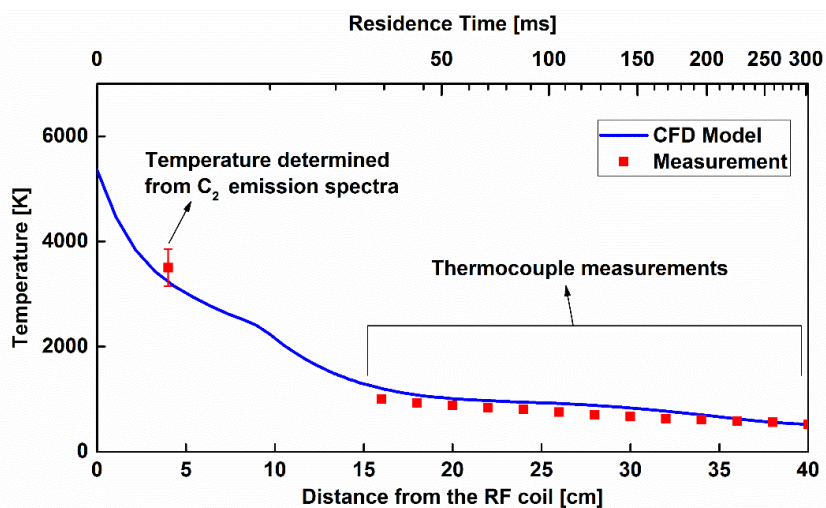


Figure 5. Comparison of measured and calculated temperature distributions as a function of distance away from the RF coil along the flow reactor.

The gas temperature at 4 cm was determined using C₂ emission measurements. We used other analytes (e.g. AlO, Fe) in our previous works^{17,33}, determined the temperature values between the 4 and 16 cm locations, and showed that the CFD model predictions were in good agreement with the experimental

results. Since the plasma flow reactor is a steady state system, residence time of the species is dependent on the axial position, which in turn is dependent on flow velocity. As a result, the CFD model was also used to infer time dependent temperature (plotted in the top x-axis of Figure 5). The cooling time scales were on the order of milliseconds (e.g. $\Delta t = 4$ ms for $\Delta x = 4$ cm and $\Delta t = 100$ ms for $\Delta x = 25$ cm). This temperature profile was used to constrain the chemical kinetics and equilibrium simulations described below. Note that a previously proposed laser inertial fusion engine specifies ~ 100 ms heating and cooling cycles^{10,11}. Therefore, the time scales of our plasma flow reactor experiments are relevant to characterize fusion engine carbon/oxygen chemistry and chemical kinetics.

4.1 Results (without oxygen)

The importance of rapid cooling on the formation of acetylene vs. carbon containing products including carbon monoxide was evaluated using chemical equilibrium and kinetics simulations. The first set of models were run for a system of carbon and hydrogen atoms without oxygen. The simulation results shown in Figures 6 (a) and (b) were obtained for an initial C_2H_2 gas input concentration of 270 ppm. The acetylene is completely atomized in the plasma and the concentrations of C and H decrease as the temperature drops along the flow reactor and new compounds are formed. Equilibrium calculations predict a peak concentration of acetylene of approximately 180 ppm from recombination reactions, followed by rapid decomposition to form aromatic species with one (e.g. C_6H_6) or two rings ($C_{10}H_8$), as shown in Figure 6 (b). Note that naphthalene ($C_{10}H_8$) was the heaviest hydrocarbon species included in the models. In contrast to the equilibrium calculations, kinetic calculations predict that C_2H_2 concentration will reach a steady state without any decomposition after recombination occurs. Also, according to the kinetic model predictions, there is a slight delay in the early recombination of carbon and hydrogen atoms. The steady state concentration of acetylene corresponds to 33% of its initial concentration.

The equilibrium calculations predict that molecular hydrogen recombines with aromatic species to form methane, the most stable hydrocarbon species at low temperatures. The other major products of the system such as polyynes with alternating single/triple bonds (e.g. C_4H_2 and C_6H_2) are included in the figures for comparison. In summary, the C_2H_2 concentration calculated by the equilibrium model would be negligible at the end of the reaction sequence and the formation of polyaromatic species and methane would be favored. However, the kinetics model predictions deviate from the equilibrium calculations, suggesting a finite rate approach is needed to model the chemical evolution of this fast cooling system.

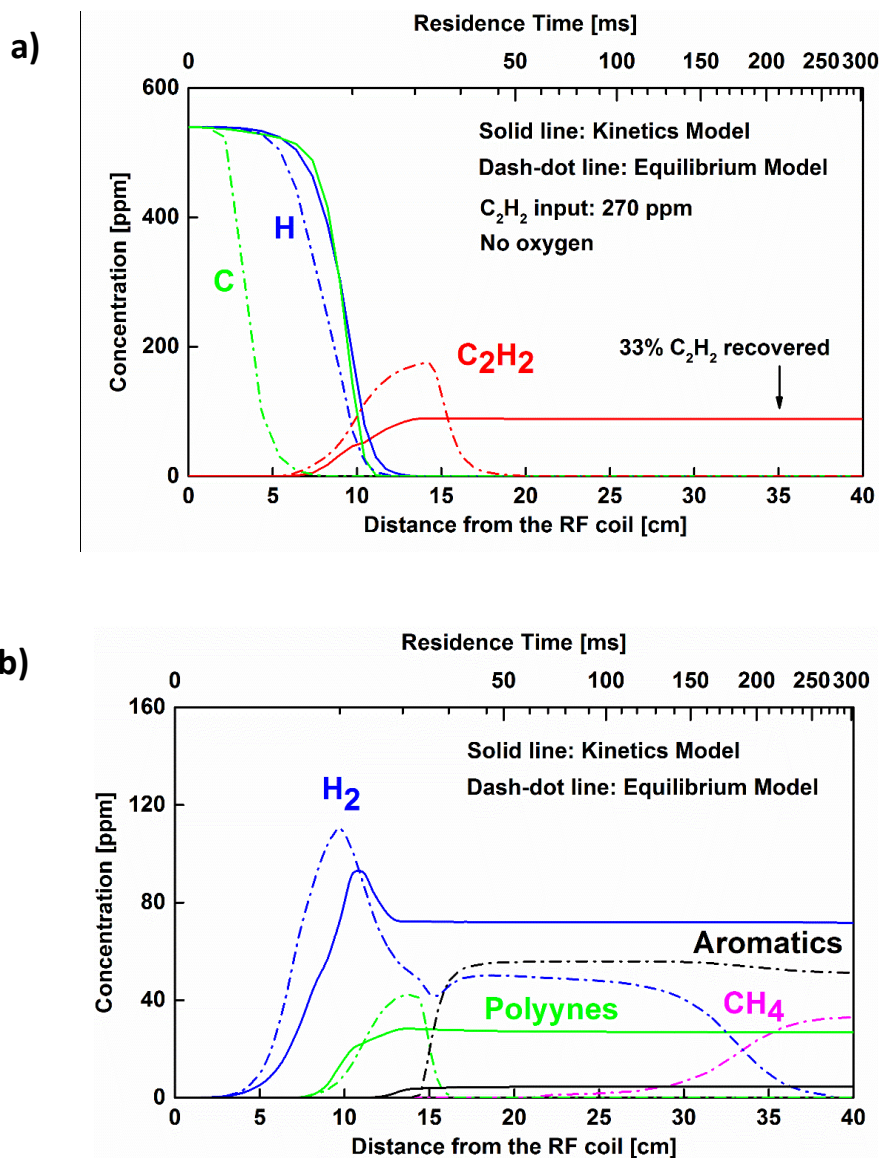


Figure 6. Comparison of concentration predictions obtained from the equilibrium and chemical kinetics models for (a) C, H, and C₂H₂ and (b) H₂, CH₄, polyynes (C₄H₂+C₆H₂), and aromatics (C₁₀H₈+C₆H₆). The residence time is given for the kinetic model predictions.

Experimental measurements of the recombined acetylene concentration were performed at two positions (16 and 116 cm) along the flow reactor axis, where corresponding temperatures were 950 K and 320 K, respectively. The measurements were repeated for different initial concentrations of C₂H₂ and the results are shown in Figure 7. The kinetics model predictions are also included in the figure, showing excellent agreement with the experimental results. Note that 33% of the input C₂H₂ recombines downstream of the reactor and the recombined amount does not change below 950 K (16 cm along the flow axis) as predicted by the kinetics model.

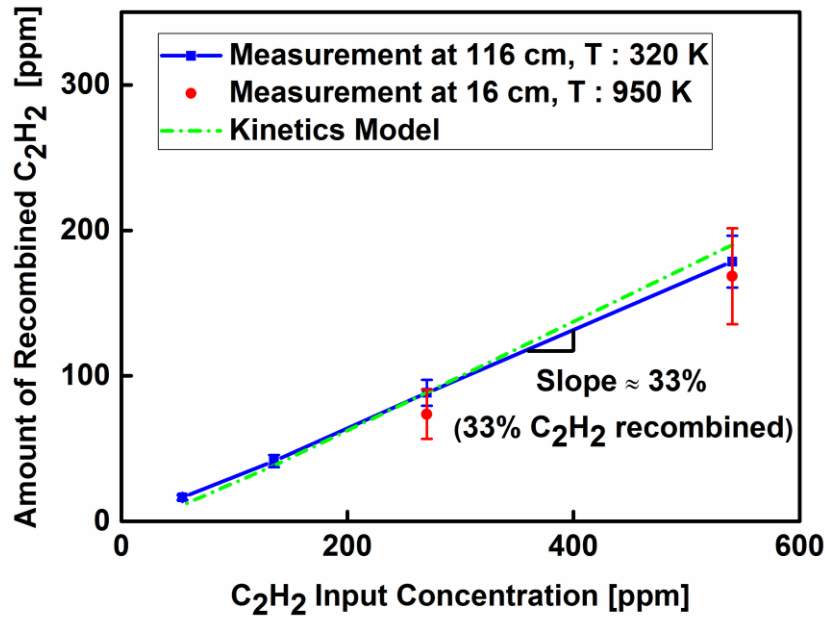


Figure 7. Amount of recombined acetylene downstream of the RF generator as a function of input concentration of acetylene.

Based on the Beer Lambert law (Eq. 1), the uncertainty of the mole fraction measurement is dependent on the errors in the measurements of absorbance, absorption cross-section, temperature, pressure, and path length. The overall uncertainties in C_2H_2 mole fraction was calculated previously¹⁷ and determined as $\pm 7\%$. However, larger error bars are plotted in Figure 7 for the 16 cm position measurements. The reason is that we observed variations in the measured temperatures at 16 cm, when the thermocouple was moved from the center of the flow field ($T \sim 1000$ K) to the walls ($T \sim 900$ K). As a result, the absorption cross sections were calculated at 900 K and 1000 K to predict the uncertainty in the mole fraction measurements calculated using the line of sight (through the entire flow tube cross section) absorbance measurement at 16 cm. The resulting uncertainty in the mole fraction was estimated as $\pm 20\%$.

4.2 Results (with oxygen)

Equilibrium and kinetic model predictions are shown in Figures 8 (a) and (b) for a system containing carbon, hydrogen, and oxygen atoms. The input concentrations of C_2H_2 and O_2 are 270 and 135 ppm, respectively. The addition of oxygen atoms to the system results in the formation of carbon-monoxide. Based on the equilibrium calculations, CO is expected to form at temperatures higher than 4500 K (Figure 8 (a)), while the kinetic model suggests the CO concentration gradually increases until 10 cm past the RF coil ($\Delta t \sim 10$ ms) where $T \sim 2000$ K. This behavior is consistent

with the multistep formation of CO. While H radicals recombine to form H₂, C atoms react with H₂ and form H and CH. Oxygen reacts with H and forms the OH radical. The OH radical is then responsible for the oxidation of C to CO and the regeneration of a H radical. This complex mechanism also explains why the H concentration sharply decreases only after all the carbon atoms are consumed and this cycle is interrupted.

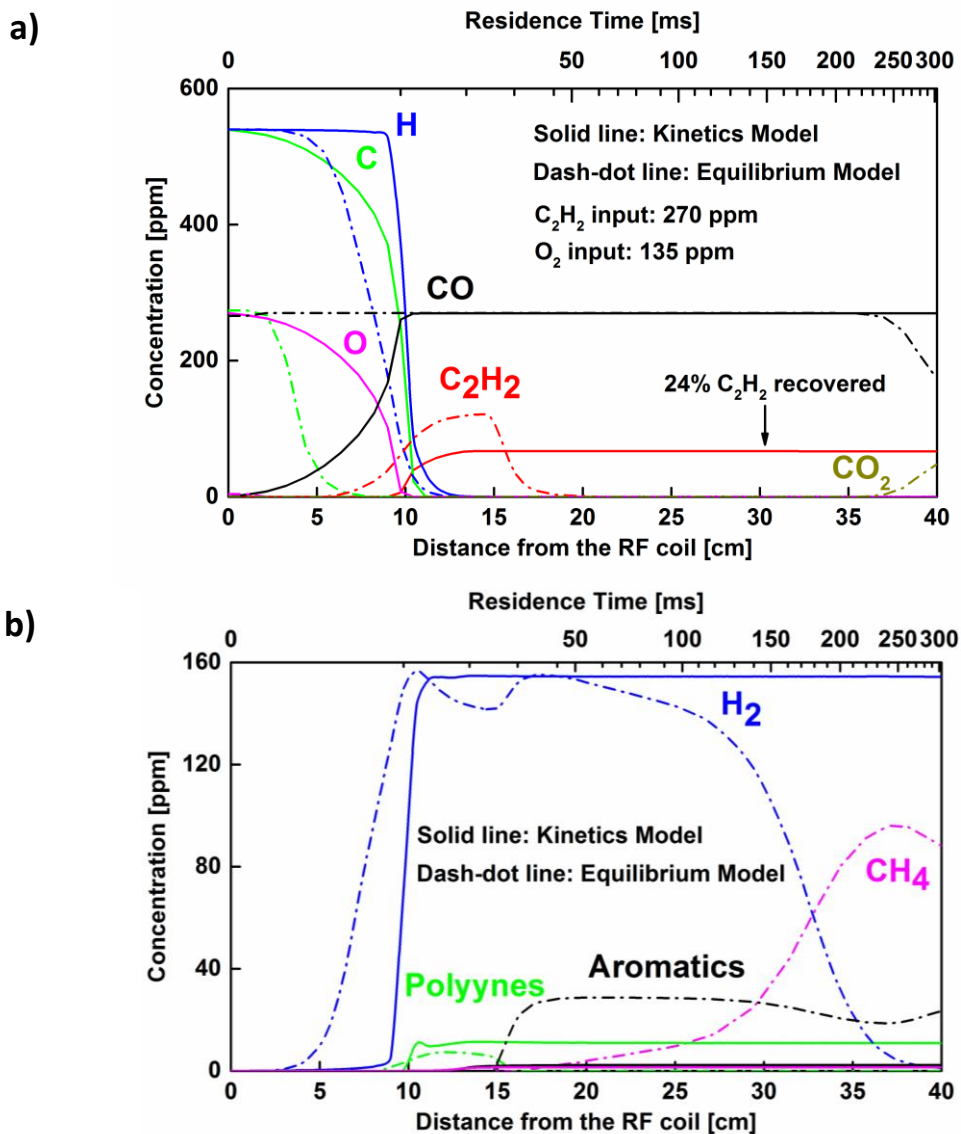


Figure 8. Comparison of concentration predictions obtained from the equilibrium and chemical kinetics models for (a) C, H, O, CO, CO₂, and C₂H₂; (b) H₂, CH₄, polyynes (C₄H₂+C₆H₂), and aromatics (C₁₀H₈+C₆H₆). The residence time is given for the kinetic model predictions. Note that the atomic oxygen concentration obtained from the equilibrium model is very small even at high temperatures (i.e. upstream of the flow reactor), because CO is the thermodynamically favored species under those conditions.

The variation in acetylene concentration in Figure 8 (a) is similar to that in Figure 6 (a). That is, C₂H₂ formation is delayed compared to the equilibrium predictions, but reaches a steady state

at temperatures below ~ 1500 K ($x > 14$ cm). The amount of C_2H_2 recovered downstream of the reactor is 24% of the initial C_2H_2 concentration. Another remarkable difference between the equilibrium and kinetic model predictions is the lack of further CO oxidation to CO_2 in the kinetic calculations. Both models also predict a decrease in the aromatic and polyene concentrations when compared to the results shown in Figure 6 (b) due to the presence of oxygen.

Experimental measurements of the recombined acetylene concentration were also performed when both C_2H_2 and O_2 were injected into the argon plasma. The measurements were taken at $T = 320$ K ($x = 116$ cm) and are plotted as a function of oxygen concentration for an initial C_2H_2 concentration of 270 ppm. The results are shown in Figure 9. The predictions of the kinetics model show good agreement with the measurement results. The measured concentration of recombined C_2H_2 was 14 ppm when a stoichiometric quantity of oxygen was input to the reactor (i.e. $X_{C_2H_2}/X_{O_2} = 1$). Further increase in the oxygen concentration prevented the recombination of C_2H_2 molecules.

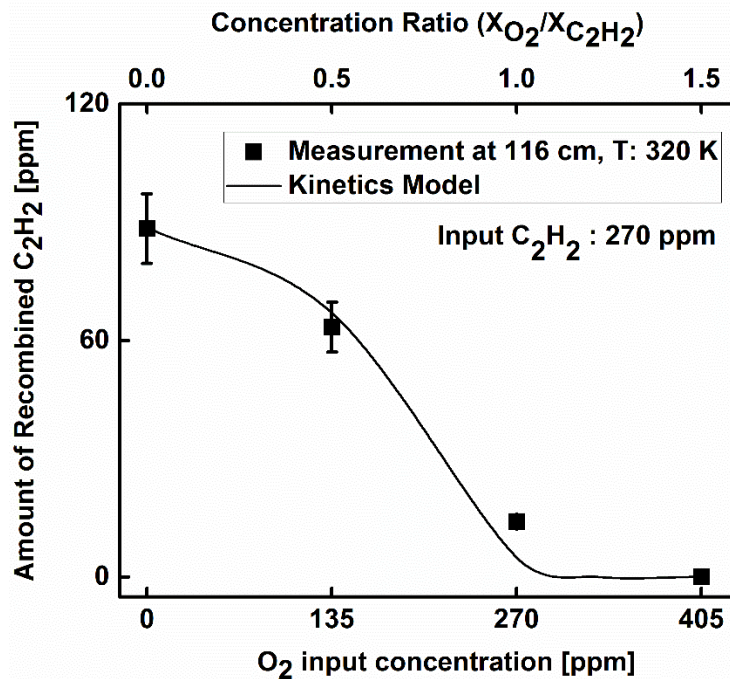


Figure 9. Amount of recombined acetylene, C_2H_2 as a function of oxygen concentration. The measurement results are compared to the kinetics model predictions. Top and bottom x-axes are given as a function of stoichiometry ($X_{O_2}/X_{C_2H_2}$) and input oxygen amount, respectively.

The area underneath the broadband molecular C_2 emission shown in Figure 3 was integrated between 440 and 580 nm and plotted in Figure 10 as a function of oxygen concentration. The normalized C_2 emission intensity decreased sharply with increasing oxygen due to the formation of CO, as predicted by the kinetics model. Since the amount of carbon in proposed laser-based

fusion engines is expected to be low¹⁰, the emission measurements were performed for two different input concentrations of acetylene: 270 ppm and 38 ppm. The O_2/C_2H_2 concentration ratio required to fully consume the diatomic carbon was the same for both experiments (Figure 10). Therefore, it can be inferred that the reaction kinetics remained the same for lower initial concentrations of the analyte. Also, note that the normalized C_2 emission intensity shown in Figure 10 shows a trend very similar to that in Figure 9 for C_2H_2 molecules. Therefore, there is a clear correlation between the diatomic carbon emission measurement results taken upstream of the reactor ($x = 4\text{cm}$) and the acetylene infrared absorption spectra results recorded downstream of the reactor ($x = 116\text{ cm}$).

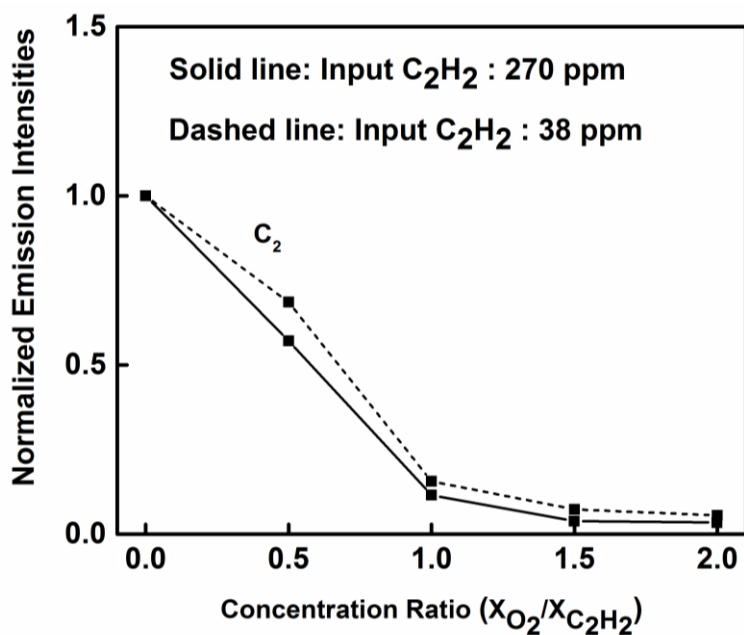


Figure 10. Variation of normalized emission intensity as a function of stoichiometry, $X_{O_2}/X_{C_2H_2}$. The results are shown for two different input concentrations of acetylene: 270 and 38 ppm.

4.3 Reaction Sensitivity and Rate of Production Analyses

In our kinetic model we included several hundred reactions to accurately describe the high temperature chemical evolution from atomic species to the acetylene molecule and then to larger hydrocarbons (e.g. C_6H_6 , $C_{10}H_8$) at cooler temperatures downstream of the flow reactor. However, only a small number of reactions contribute to the acetylene production/consumption. A sensitivity and a rate of production analyses are required to identify those most important chemical pathways controlling the acetylene yield in our experiments.

The sensitivity analysis enables quantitative understanding of how the acetylene concentration ($\chi_{C_2H_2}$) depends on the reaction rates (k_i) employed in the kinetic model. The analysis requires calculating the sensitivity coefficients (S) using the following formula

$$S(\chi_{C_2H_2}, k_i, t) = \left\{ \frac{d\chi_{C_2H_2}(t)}{dk_i} \right\} \left\{ \frac{k_i}{\chi_{C_2H_2}(t)} \right\} \quad (3)$$

The temperature distribution shown in Figure 5 was input to CHEMKIN PRO⁴⁹ to calculate the sensitivity coefficients for input carbon and hydrogen concentrations of 540 ppm and oxygen concentration of 270 ppm, respectively. The acetylene amount was determined to be most sensitive to the reactions shown in Figure 11. The results are given as a function of temperature (bottom x-axis) and residence time (top x-axis) along the flow reactor. Acetylene concentration is most sensitive to the dissociative/recombination reactions involving radical species such as C, H, CH, and CH₂ (Rxn#1 to Rxn #8). Those reactions have positive sensitivity coefficients, contributing to the production of C₂H₂ molecules. The other two reactions (Rxn#9 and Rxn #10) involve OH, O, and HCCO radicals and have negative sensitivity coefficients, favoring the consumption of C₂H₂ molecules.

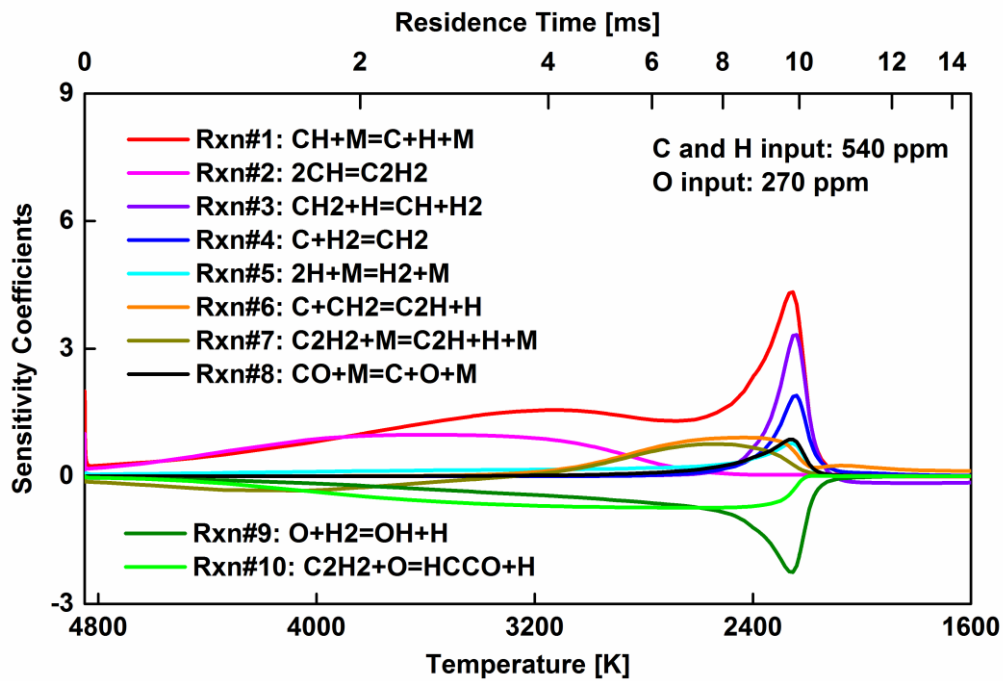


Figure 11. Reaction sensitivity analysis for the rate-determining steps that affect C₂H₂ formation. The sensitivity coefficients defined in Eq. (3) were obtained from Chemkin⁴⁹ simulations using input carbon and hydrogen concentrations of 540 ppm and oxygen concentration of 270 ppm, respectively.

Fig. 11 shows that the acetylene concentration is most sensitive to the reaction rates when the gas temperature drops to 2250 K at $t = 9.9$ ms. That time corresponds to the steepest rise in C_2H_2 production according to the results displayed in Fig. 8 (a). Therefore, the acetylene rate of production analysis was performed at 2250 K to determine the major pathways that account for the acetylene production/consumption. The results are displayed in Fig. 12. The absolute rate values ($\text{mole}/\text{cm}^3\text{s}$) are given along the x-axis of the figure together with their corresponding percentages written next to each reaction. The ten reactions given in the figure sum up to 97% of the acetylene net production. There are two reactions common to the results of the sensitivity and rate of production analyses. Those are Rxn #2 and Rxn #10. The reactions between acetylene and atomic oxygen (i.e. Rxn #10 and 11) have negative rate values and are the main consumption channels, whereas the radical recombination reactions (i.e. Rxn #2, 17, and 18) account for most of the acetylene production.

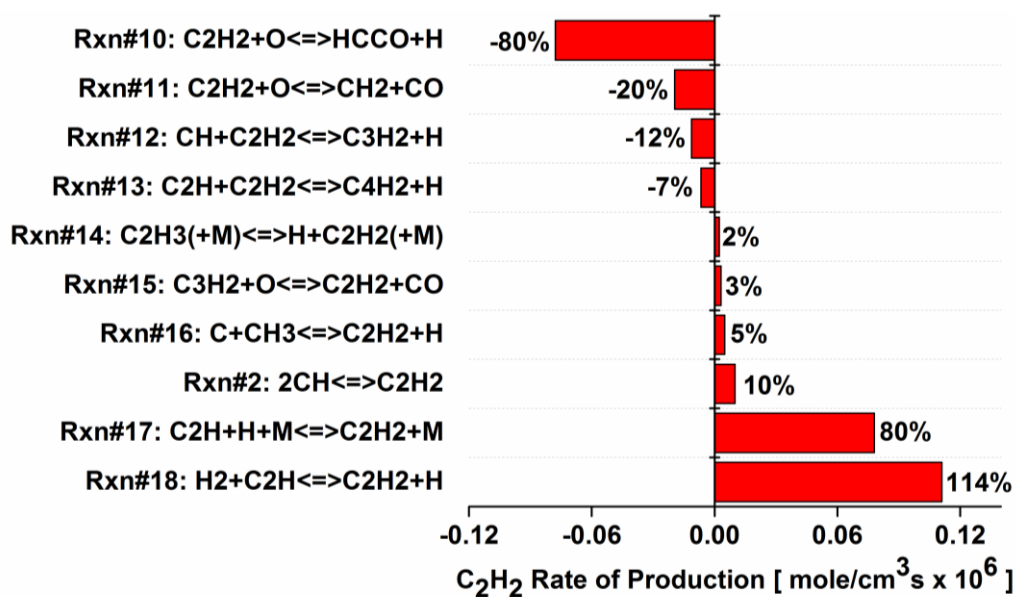


Figure 12. Dominant reactions that produce/consume C_2H_2 molecule. The absolute rate values are given along the x-axis for each reaction in addition to their corresponding percentages. The ten reactions given in the figure add up to 97% of the acetylene net production.

The results of the sensitivity and rate of production analyses indicate that there are only a few reactions in the kinetic model (e.g. Rxn # 1, 2, 10, 17, and 18) that control the rate and amount of acetylene formation. Therefore, the error in acetylene concentration prediction highly depend on the uncertainty of those reaction rates. Those rates were studied extensively^{36,37,52-54} and most of them were measured experimentally (e.g. $\pm 25\%$ uncertainty³⁷). In this study, the accuracy of

the current model predictions is validated by the experimental C_2H_2 concentration measurements. The uncertainty of the model predictions could be further improved in future studies by comparison of the predictions to measurements of the other major products (e.g. CO).

5. CONCLUSION

In this study, a recently developed plasma flow reactor was used to perform experiments at relatively fast cooling time scales similar to the outer regions of an ignition chamber of fusion energy devices¹⁰. The idea of using oxygen together with carbon to prevent activated carbon deposition on the fusion reactor chamber walls was tested by injecting acetylene gas into the argon plasma, decomposing it into its constituent elements, and investigating the recombination chemistry during the rapid cooling of the carbon/hydrogen system in high/low oxygen environments. Since acetylene is the key hydrocarbon precursor to soot formation, we monitor acetylene formation as a function of location (i.e. temperature) in our plasma flow reactor to investigate the proposed method of preventing carbon dust formation in ICF environments¹⁰ via oxygen addition to the input stream of gasses.

The early chemical evolution from atomic to diatomic carbon was monitored upstream of the reactor ($x = 4$ cm at $t = 4$ ms) by means of UV/VIS emission spectroscopy at high temperatures ($T \sim 3500$ K). Infrared absorption spectroscopy at lower temperatures ($T \sim 1000$ K) was used to measure the concentration of the soot precursor (i.e. acetylene) downstream of the flow reactor ($x = 16$ at $t = 30$ ms). A detailed kinetic model, constrained by experimental results, was assembled to investigate the competing reactions, rate limiting steps, and the associated time scales for the formation of C/H products including aromatics, polyynes, and acetylene as well as the formation of carbon-monoxide in oxidizing environments.

In both experiments and kinetics modelling, we find that, after complete decomposition, 33% of C_2H_2 gas input to the argon plasma recombines downstream of the reactor within 20 ms, when there is no oxygen in the system. The addition of oxygen in 1:1 proportion to carbon strongly favors the formation of CO in 10 milliseconds and prevents the formation of diatomic carbon and C_2H_2 molecules upstream and downstream of the reactor, respectively. The kinetic model also enabled the identification of the most important pathways controlling the acetylene yield through reaction sensitivity and rate of production analyses.

The carbonaceous particle formation in fusion energy reactors is a complex process that involves multiple sequences of chemical reactions which can show variations depending on the

plasma conditions (e.g. pressure, temperature, feed gas). As a result, there is not a single comprehensive kinetic model in the literature that can predict the amount and rate of carbon dust formation in fusion energy reactors. Given the significance of acetylene as a precursor to carbonaceous particle formation and the paucity of studies in the nuclear fusion literature to understand the chemical pathways resulting in soot formation from gaseous hydrocarbons, the current study is a significant contribution to investigating the chemical-based mitigation strategies for eliminating the formation of detrimental carbon dust in fusion energy reactors.

ACKNOWLEDGMENTS

Funding was provided by Laboratory Directed Research and Development (LDRD) grants 14-ERD-077 (M. Armstrong, PI) and 16-ERD-008 (T. Rose, PI). We acknowledge useful conversations with Mark A. Cappelli, Mike Dunne, Tom Anklam, Wayne Meier, Susana Reyes, Robin Miles, and Kevin Kramer. This work was performed under the auspices of the U.S. Department of Energy by Lawrence Livermore National Laboratory under Contract DE-AC52-07NA27344.

6. REFERENCES

1. Baron-Wiechec, A. *et al.* First dust study in JET with the ITER-like wall: Sampling, analysis and classification. *Nuclear Fusion* **55**, (2015).
2. Rubel, M. *et al.* Dust particles in controlled fusion devices: morphology, observations in the plasma and influence on the plasma performance. *Nuclear Fusion* **41**, (2001).
3. Widdowson, A. *et al.* Comparison of JET main chamber erosion with dust collected in the divertor. *Proc. 20th Int. Conf. Plasma-Surf. Interact. Control. Fusion Devices* **438**, S827–S832 (2013).
4. Smirnov, R. D., Krasheninnikov, S. I., Pigarov, A. Y. & Rognlien, T. D. Tungsten dust impact on ITER-like plasma edge. *Phys. Plasmas* **22**, 012506 (2015).
5. Winter, J. Dust in fusion devices - experimental evidence, possible sources and consequences. *Plasma Physics and Controlled Fusion* **40**, (1998).
6. Sharpe, J. ., Petti, D. . & Bartels, H.-W. A review of dust in fusion devices: Implications for safety and operational performance. *Fusion Eng. Des.* **63–64**, 153–163 (2002).
7. Kovačević, E., Stefanović, I., Berndt, J. & Winter, J. Infrared fingerprints and periodic formation of nanoparticles in Ar/C₂H₂ plasmas. *J. Appl. Phys.* **93**, 2924–2930 (2003).
8. Krasheninnikov, S. I., Smirnov, R. D. & Rudakov, D. L. Dust in Magnetic Fusion Devices. *Plasma Physics and Controlled Fusion* (2011).
9. Hong, S., Berndt, J. & Winter, J. Growth precursors and dynamics of dust particle formation in the Ar/CH₄ and Ar/C₂H₂ plasmas. *Plasma Sources Science and Technology* **12**, (2002).
10. Latkowski, J. F. *et al.* Chamber Design for the Laser Inertial Fusion Energy (LIFE) Engine. *Fusion Sci. Technol.* **60**, 54–60 (2011).
11. Lindl, J. Development of the indirect-drive approach to inertial confinement fusion and the target physics basis for ignition and gain. *Phys. Plasmas* **2**, 3933–4024 (1995).
12. Vathy, A. *et al.* Tokamak-like dust removal induced by laser irradiation. *Proc. 19th Int. Conf. Plasma-Surf. Interact. Control. Fusion* **415**, S1115–S1118 (2011).

13. Wolowski, J. *et al.* Study of laser-induced removal of co-deposits from tokamak plasma-facing components using ion diagnostics and optical spectroscopy. *Radiat. Eff. Defects Solids* **165**, 434–440 (2010).
14. Davis, J. W., Fitzpatrick, B. W. N., Sharpe, J. P. & Haasz, A. A. Thermo-oxidation of tokamak carbon dust. *Fusion React. Mater.* **386–388**, 764–767 (2009).
15. Philipps, V. *et al.* Removal of carbon layers by oxygen glow discharges in TEXTOR. *Plasma-Surf. Interact.-17* **363–365**, 929–932 (2007).
16. Paci, S. & Porfiri, M. T. Experimental and numerical analysis of the air inflow technique for dust removal from the vacuum vessel of a tokamak machine. *Fusion Eng. Des.* **83**, 151–157 (2008).
17. Koroglu, B. *et al.* Plasma flow reactor for steady state monitoring of physical and chemical processes at high temperatures. *Rev. Sci. Instrum.* **88**, 093506 (2017).
18. Frenklach, M. Reaction mechanism of soot formation in flames. *Physical Chemistry Chemical Physics* (2002).
19. Appel, J., Bockhorn, H. & Frenklach, M. Kinetic modeling of soot formation with detailed chemistry and physics: laminar premixed flames of C2 hydrocarbons. *Combust. Flame* **121**, 122–136 (2000).
20. Krestinin, A. V. Detailed modeling of soot formation in hydrocarbon pyrolysis. *Combust. Flame* **121**, 513–524 (2000).
21. Sánchez, N. E., Callejas, A., Millera, A., Bilbao, R. & Alzueta, M. U. Formation of PAH and soot during acetylene pyrolysis at different gas residence times and reaction temperatures. *2nd Int. Meet. Clean. Combust. CM0901-Detail. Chem. Models Clean. Combust.* **43**, 30–36 (2012).
22. Saggese, C. *et al.* Kinetic Modeling Study of Polycyclic Aromatic Hydrocarbons and Soot Formation in Acetylene Pyrolysis. *Energy Fuels* **28**, 1489–1501 (2014).
23. Apicella, B. *et al.* Separation and characterization of carbonaceous particulate (soot and char) produced from fast pyrolysis of coal in inert and CO2 atmospheres. *1st Int. Workshop Oxy-Fuel Combust.* **201**, 118–123 (2017).
24. Aggadi, N. *et al.* Structural and chemical characterisation of soot particles formed in Ar/H2/CH4 microwave discharges during nanocrystalline diamond film synthesis. *Diam. 2005* **15**, 908–912 (2006).
25. Arnas, C. *et al.* Similarities and differences between dust produced in laboratory plasmas and in the MAST and Tore Supra tokamaks. *Plasma Physics and Controlled Fusion* **52**, (2010).
26. Mao, M., Benedikt, J., Consoli, A. & Bogaerts, A. New pathways for nanoparticle formation in acetylene dusty plasmas: a modelling investigation and comparison with experiments. *Journal of Physics D: Applied Physics* **41**, (2008).
27. Peng, Y., Lacroix, D., Hugon, R., Brosset, C. & Bougdira, J. Experimental and theoretical investigations of absorbance spectra for edge-plasma monitoring in fusion reactors. *J. Quant. Spectrosc. Radiat. Transf.* **109**, 1549–1562 (2008).
28. Dap, S., Lacroix, D., Hugon, R. & Bougdira, J. Retrieving particle size and density from extinction measurement in dusty plasma, Monte Carlo inversion and Ray-tracing comparison. *Eurotherm Semin. Comput. Therm. Radiat. Particip. Media IV* **128**, 18–26 (2013).
29. Stranic, I. & Hanson, R. K. Laser absorption diagnostic for measuring acetylene concentrations in shock tubes. *J. Quant. Spectrosc. Radiat. Transf.* **142**, 58–65 (2014).
30. Lam, J. *et al.* Investigation of local thermodynamic equilibrium in laser-induced plasmas: Measurements of rotational and excitation temperatures at long time scales. *Spectrochim. Acta Part B At. Spectrosc.* **101**, 86–92 (2014).
31. Bruggeman P. J. , Sadeghi B. , Schram D. C. , Linss V. Gas temperature determination from rotational lines in non-equilibrium plasmas: a review. *Plasma Sources Sci. Technol.* **23**, (2014).
32. Calculation of ground state rotational populations for kinetic gas homonuclear diatomic molecules including electron-impact excitation and wall collisions. *J. Chem. Phys.* **133**, 094303 (2010).

33. Koroglu, B. *et al.* Gas Phase Chemical Evolution of Uranium, Aluminum, and Iron Oxides. *Sci. Rep.* **8**, 10451 (2018).
34. Parigger, C. G. *et al.* Computation of diatomic molecular spectra for selected transitions of aluminum monoxide, cyanide, diatomic carbon, and titanium monoxide. *Spectrochim. Acta Part B At. Spectrosc.* **107**, 132–138 (2015).
35. Hanson, R. K. Shock-tube study of carbon monoxide dissociation kinetics. *J. Chem. Phys.* **60**, 4970–4976 (1974).
36. Braun, W., McNesby, J. R. & Bass, A. M. Flash Photolysis of Methane in the Vacuum Ultraviolet. II. Absolute Rate Constants for Reactions of CH with Methane, Hydrogen, and Nitrogen. *J. Chem. Phys.* **46**, 2071–2080 (1967).
37. Dean, A. J. & Hanson, R. K. CH and C-atom time histories in dilute hydrocarbon pyrolysis: Measurements and kinetics calculations. *Int. J. Chem. Kinet.* **24**, 517–532 (1992).
38. Harding, L. B., Guadagnini, R. & Schatz, G. C. Theoretical studies of the reactions $H + CH \rightarrow C + H_2$ and $C + H_2 \rightarrow CH_2$ using an ab initio global ground-state potential surface for CH_2 . *Journal of Physical Chemistry* **97(21)**, 5472–5481 (1993).
39. Kruse, T. & Roth, P. Kinetics of C2 Reactions during High-Temperature Pyrolysis of Acetylene. *J. Phys. Chem. A* **101**, 2138–2146 (1997).
40. Mayer, S. W., Schieler, L. & Johnston, H. S. Computation of high-temperature rate constants for bimolecular reactions of combustion products. *Symp. Int. Combust.* **11**, 837–844 (1967).
41. MICK, H.-J., BURMEISTER, M. & ROTH, P. Atomic resonance absorption spectroscopy measurements on high-temperature CO dissociation kinetics. *AIAA J.* **31**, 671–676 (1993).
42. Husain, D. & Kirsch, L. J. Reactions of atomic carbon by kinetic absorption spectroscopy in the vacuum. *Transactions of The Faraday Society* **67**, (1971).
43. Husain, D. & Young, A. N. Kinetic investigation of ground state carbon atoms, C(23P). *J. Chem. Soc. Faraday Trans. 2 Mol. Chem. Phys.* **71**, 525–531 (1975).
44. Miller, J. A. & Klippenstein, S. J. The recombination of propargyl radicals and other reactions on a C6H6 potential. *J. Phys. Chem. A* **107**, 7783–7799 (2003).
45. Alzueta, M. U., Glarborg, P. & Dam-Johansen, K. Experimental and kinetic modeling study of the oxidation of benzene. *Int. J. Chem. Kinet.* **32**, 498–522 (2000).
46. Emdee, J. L., Brezinsky, K. & Glassman, I. A kinetic model for the oxidation of toluene near 1200 K. *J. Phys. Chem.* **96**, 2151–2161 (1992).
47. Marinov, N. M., Pitz, W. J., Westbrook, C. K., Castaldi, M. J. & Senkan, S. M. Modeling of Aromatic and Polycyclic Aromatic Hydrocarbon Formation in Premixed Methane and Ethane Flames. *Combust. Sci. Technol.* **116–117**, 211–287 (1996).
48. STAR-CCM+ 12.04, Siemens PLM Software: Plano. (2017).
49. ANSYS 18.0 Chemkin-Pro, ANSYS, Inc.: San Diego. (2017).
50. Koroglu, B., Pryor, O. M., Lopez, J., Nash, L. & Vasu, S. S. Shock tube ignition delay times and methane time-histories measurements during excess CO2 diluted oxy-methane combustion. *Combust. Flame* **164**, 152–163 (2016).
51. E. Goos, A. Burcat & B. Ruscic. *Extended Third Millennium Ideal Gas Thermochemical Database with updates from Active Thermochemical Tables*. <http://garfield.chem.elte.hu/Burcat/burcat.html>. (2017).
52. Eiteneer, B. & Frenklach, M. Experimental and Modeling Study of Shock-Tube Oxidation of Acetylene. *International Journal of Chemical Kinetics* **35**, 391–414 (2003).
53. Tsang, W. & Hampson, R. F. Chemical Kinetic Data Base for Combustion Chemistry. Part I. Methane and Related Compounds. *J. Phys. Chem. Ref. Data* **15**, 1087–1279 (1986).
54. Harding, L. B., Schatz, G. C. & Chiles, R. A. An ab initio determination of the rate constant for $H_2 + C_2H \rightarrow H + C_2H_2$. *J. Chem. Phys.* **76**, 5172–5173 (1982).